Electronic supplementary information (ESI)

Gradual Conductance Modulation by Defect Reorganization in Amorphous Oxide Memristor

Siqin Li,[a] Jigang Du,[b] Bojing Lu,[a] Ruqi Yang,[a] Dunan Hu,[a] Pingwei Liu,[b] Haiqing Li,[c] Jingsheng Bai,[d] Zhizhen Ye, *[a] and Jianguo Lu*[a]

[a] *State Key Laboratory of Silicon and Advanced Semiconductor Materials, School of Materials Science and Engineering, Zhejiang University, Hangzhou 310058, China*
[b] *College of Chemical and Biological Engineering, Zhejiang University, Hangzhou 310058, China*
[c] *School of Electromechanical Engineering, Guangdong University of Technology, Guangzhou 510006, China*
[d] *Sinoma Institute of Materials Research (Guang Zhou) Co., Ltd (SIMR), Guangzhou 510530, China*

*E-mail: yezz@zju.edu.cn (Zhizhen Ye), lujianguo@zju.edu.cn (Jianguo Lu).

Table of contents

Section 1. Supplementary DC *I-V* characterization

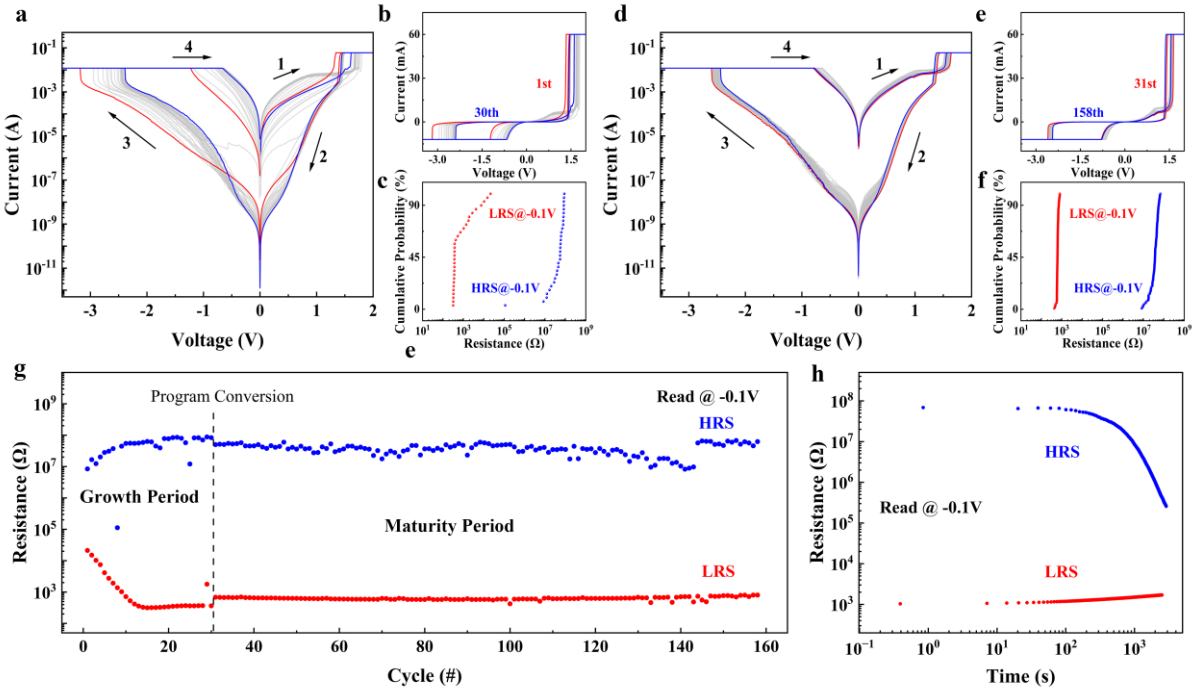

Fig. S1 DC resistive switching characteristics of Au/a-ZATO/Au memristor. (a) The so-called "growth period" of the device lasts about 30 cycles, during which the window between HRS and LRS gradually widens. The black arrows with numbers indicate the direction and sequence of voltage sweeps. (b) Corresponding linear-scale image. Red represents the 1st cycle, while blue the 30th cycle. (c) Cumulative probability from the first 30 cycles. (d)-(f) So-called "maturity period" with no remarkable fluctuations in HRS and LRS. I-V curves are highly overlapped. (g) Endurance performance exhibits an HRS/LRS ratio of more than 10^5. The dotted line indicates where the test sequences are switching. (h) Retention characteristics in HRS and LRS. The read voltage is -0.1 V.

Since a test sequence of the program in the semiconductor parameter analyzer here contains up to 128 *I-V* loops, a test larger than 128 cycles entails a “program conversion” between sequences. The switching of test sequences will introduce uncontrollable current overshoot due to the circuit design of the semiconductor parameter analyzer, which may cause the endurance test results of two adjacent sequences to be misaligned. The current overshoot phenomenon may be attributed to the parasitic capacitance between the external transistor in semiconductor parameter analyzer and the test device.[1] As shown in Fig. S1g, there is a small gap in the LRS before and after “program conversion”, as does the HRS.

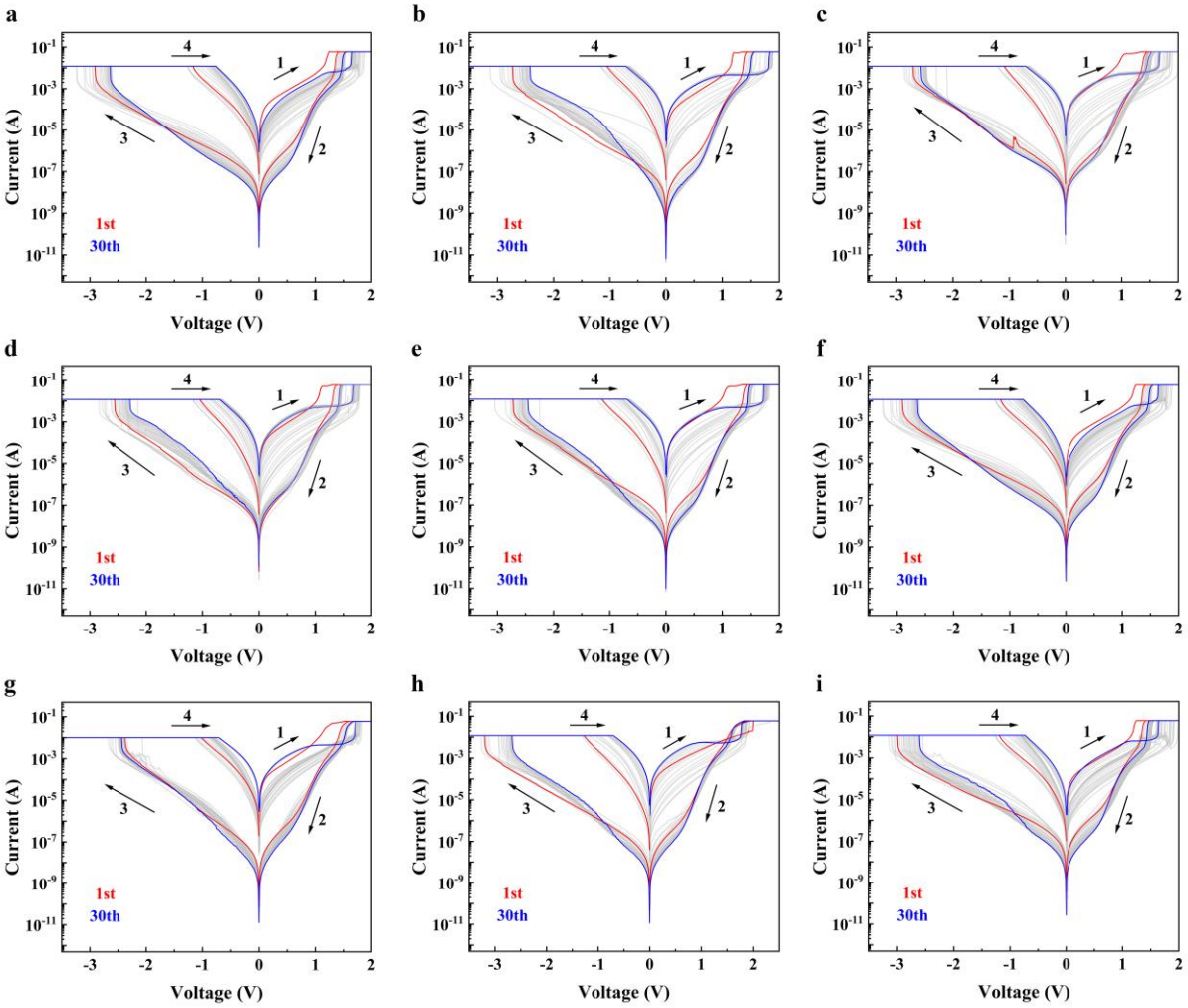

Fig. S2 Parallel device I-V (DC) characterizations illustrate device-to-device uniformity. (a)- (i) Overlay of the first 30 gradient cycles exhibit "growth period" clearly. Black arrows with number indicate the sequence and direction of voltage sweeps. The red curve represents the 1st cycle, while the blue one represents the 30th. The compliance current is 0.06 A for positive bias and 0.012 A for negative bias. Sweeping time for each cycle is about 1 min so 30 cycles is about 30 min for each device.

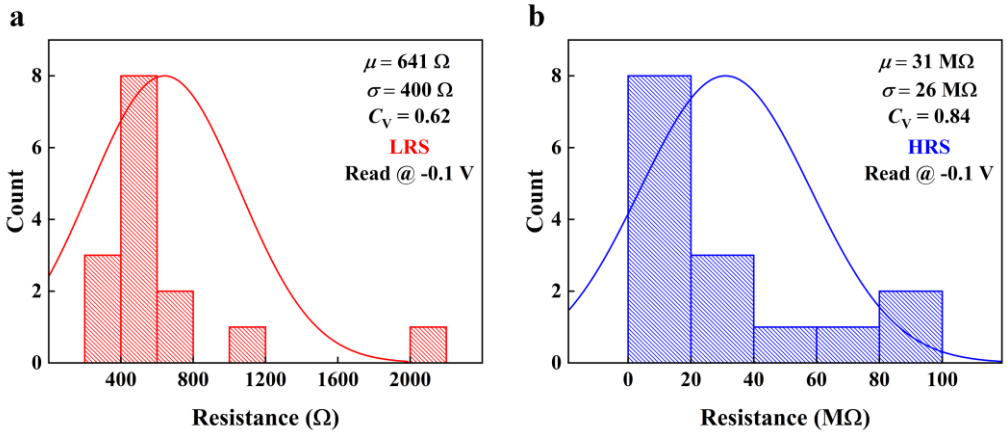

Fig. S3 Statistical analysis of device-to-device variation. Take the 30th *I-V* loop of each device (15 total) as data set. (a) The mean value (μ) of LRS is 641 Ω, the standard deviation (δ) is 400 Ω, and the coefficient of variation (C_V) is 0.62. Note that $C_V = \delta/\mu$. (b) For HRS, μ= 31 MΩ, δ= 26 MΩ, C_V =0.84. Read voltage is -0.1 V.

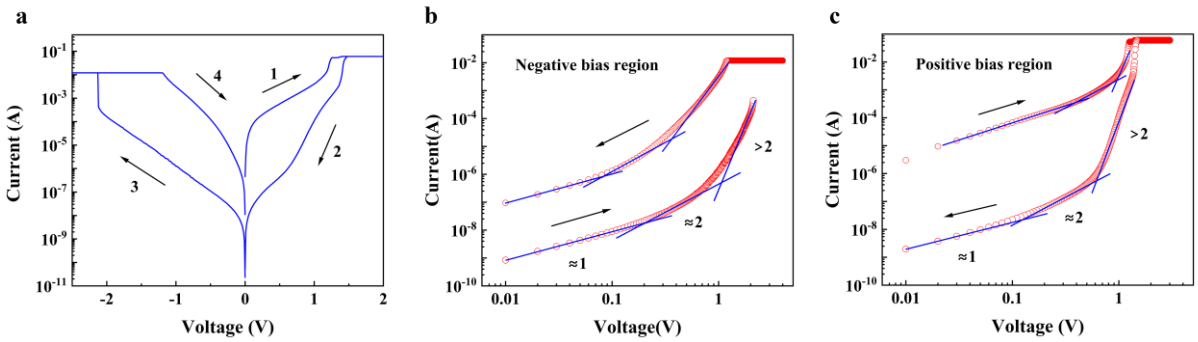

Fig. S4 Conduction mechanism of Au/a-ZATO/Au is consistent with the space charge limited conductance (SCLC) model. (a) The first pinch hysteresis loop. Black arrows indicate the direction of the voltage sweep, while the number illustrate the process sequence. (b) Double logarithmic plot of the negative voltage region. (c) Double logarithmic plot of the positive voltage region. Numbers marked in (b) and (c) are the slopes of tangent lines. Curve segment with slope of approximately 1 is from ohmic conduction. Tangent slope about 2 belong to "trap-unfilled SCLC", while slope greater than 2 are defined as "trap-filled SCLC".

The SCLC current density could be qualitatively expressed by the following formula:[2, 3]

$$J_{SCLC} \propto \begin{cases} V \\ V^2 \\ V^n, n > 2 \end{cases} \quad (1)$$

Thus, the curve segment in the double logarithmic *I-V* plot with a slope close to 1 corresponds to ohmic conduction. The "trap-unfilled SCLC" is represented by the segment with a slope about 2, while the segment with a slope greater than 2 belongs to "trap-filled SCLC".

Section 2. Pulse potentiation, pulse depression and relaxation analysis

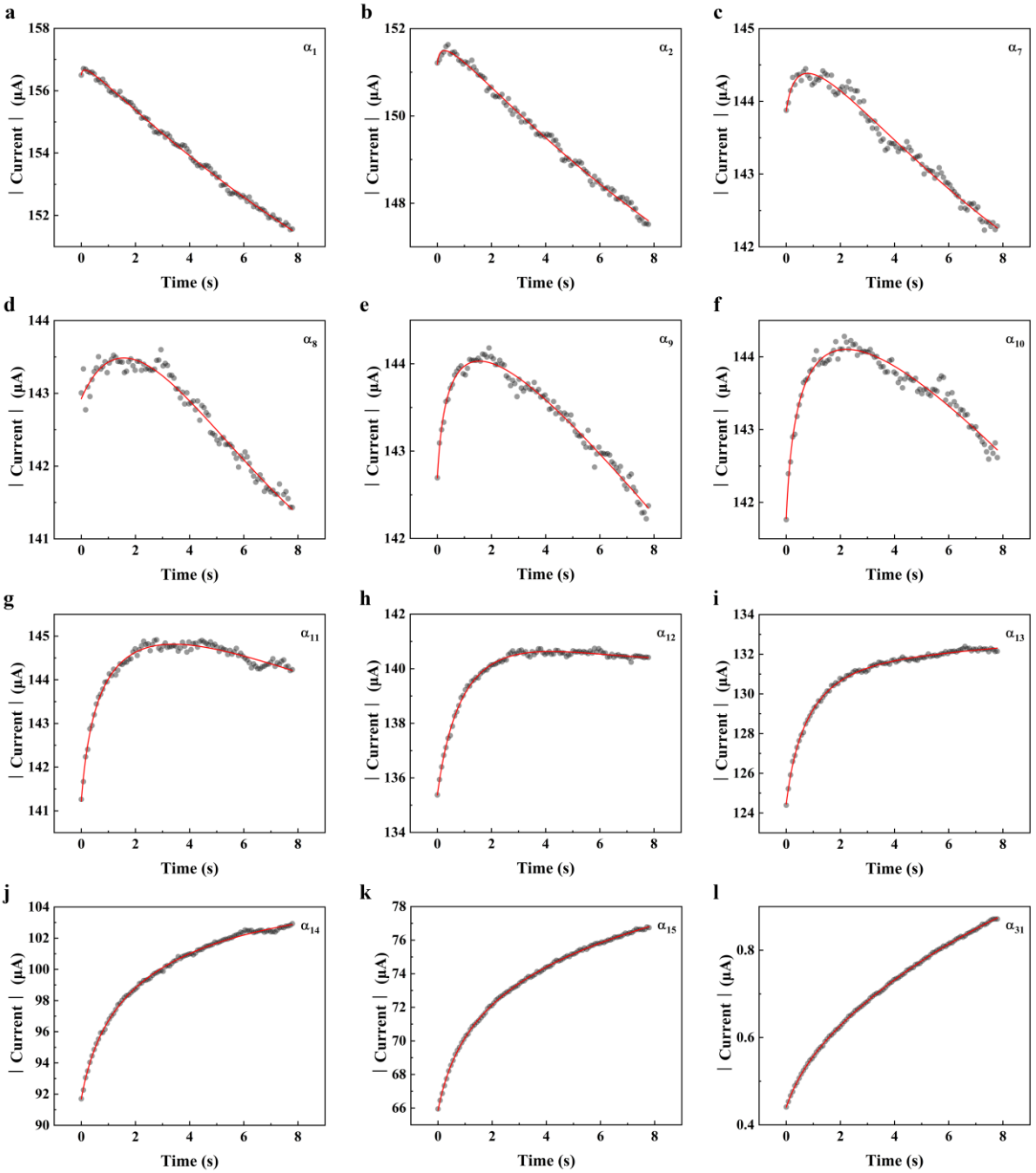

Fig. S5 Logarithmic-exponential mixed relaxation of Au/a-ZATO/Au during switching from LRS to HRS. (a)- (l) The initial current value decreased step by step. α_1-α_{31} are the labels of the relaxation processes during pulse interval. The proportion of exponential decay gradually decreases, while logarithmic growth gradually enhances simultaneously. The gray dots are data points, and the red curve is the fitting result.

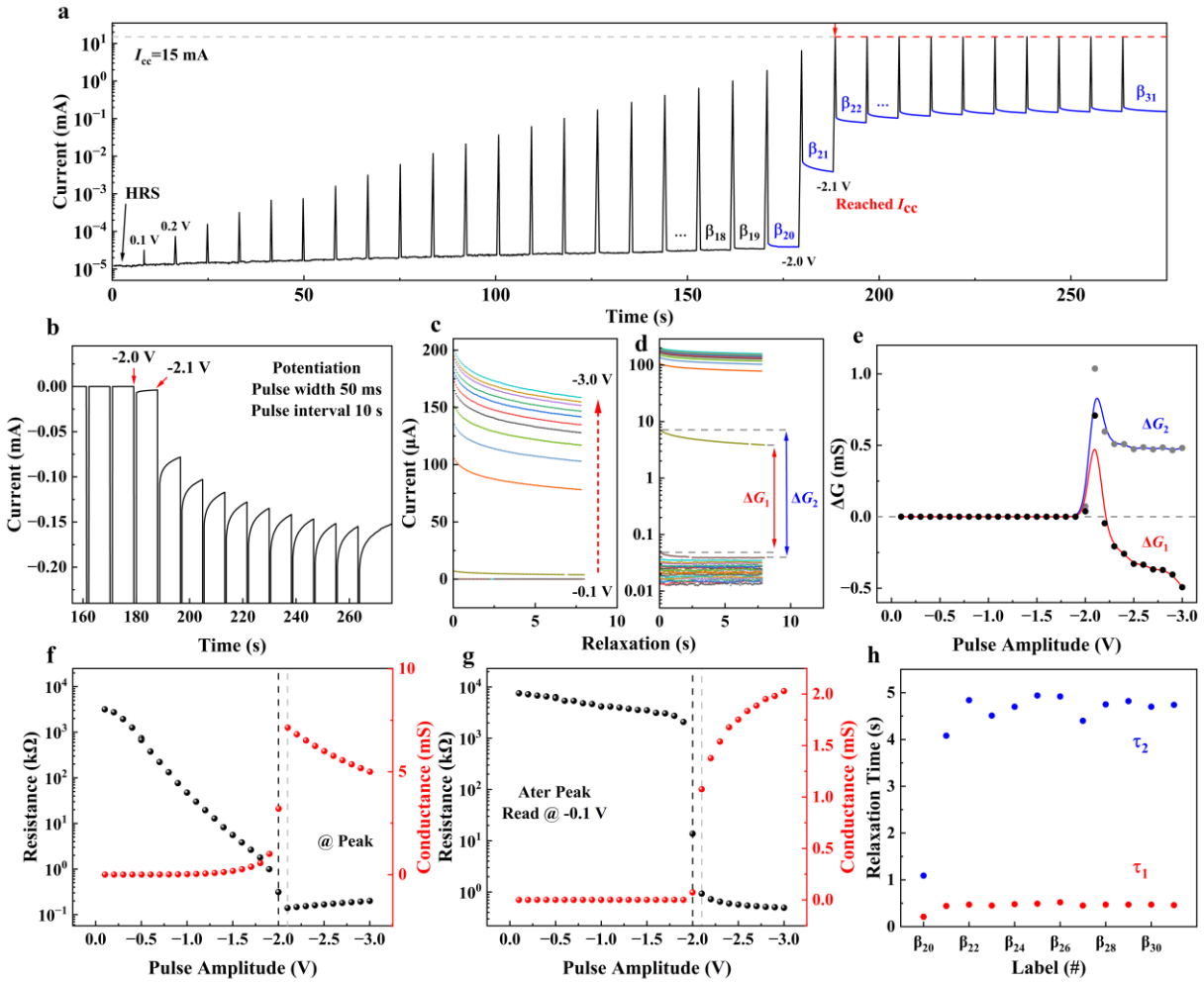

Fig. S6 Stepped conductance potentiation in excitation pulse trains. (a) *I-t* diagram starts from HRS, where current is logarithmic scale. -2.0 V pulse reaches the compliance current (15 mA), marked by red dotted line. β_1-β_{31} are labels of the relaxation process. (b) *I-t* diagram with linear scale. The width and interval of depression pulse is 50 ms and 10 s, respectively. (c) Linear and (d) Logarithmic plots are collected from relaxation processes in (a). ΔG_1 represents the difference between the conductance at the end of relaxation and the beginning conductance of the previous relaxation process. ΔG_2 represents the difference between the beginning conductance and the conductance at the end of relaxation of the previous relaxation process. Pulse amplitude was increased from -0.1 V to -3.0 V. (e) Relationship between ΔG_1 (or ΔG_2) and the potentiation amplitude. (f) Variation of peak resistance (or conductance) with pulse amplitude; (g) Variation of relaxation initial resistance (or conductance) with amplitude. The black dotted line corresponds to the -2.0 V pulse in (b), while the gray dotted line marks the pulse reached I_{cc}. (h) Development of time constant obtained by double-exponential decay fitting. Here, τ_1 and τ_2 are exponential time constant.

The double-exponential decay is fitted by the following function:[4, 5]

$$I = I_0 + I_1 \exp\left(\frac{-x}{\tau_1}\right) + I_2 \exp\left(\frac{-x}{\tau_2}\right), \tau_2 > \tau_1 \quad (2)$$

In the function, I_0, I_1 and I_2 are fitting parameters, whereas τ_1 and τ_2 are relaxation time constant of the double-exponential decay. It is stipulated that τ_2 is greater than τ_1. The relatively small

time constant τ_1 is thought to be associated with short term memory (STM), while τ_2 reveals long term memory (LTM). Some studies on photoelectric synapses have shown that the fast relaxation process may be related to the recombination of electrons and holes.[6] Here, the *I-t* diagram of the β_{19} process has exhibited an exponential decay pattern firstly, but it could not be well fitted by Equation 2. From β_{20} to β_{21}, the time constant τ_2 sees a significant increase from about 1 s to 4 s, while the rise of τ_1 is less than 0.5 s. During the subsequent β_{22} to β_{31} process, τ_1 and τ_2 are almost stable. It implies that the device has been switched to LRS, wherein stronge conductive structures have been constructed.

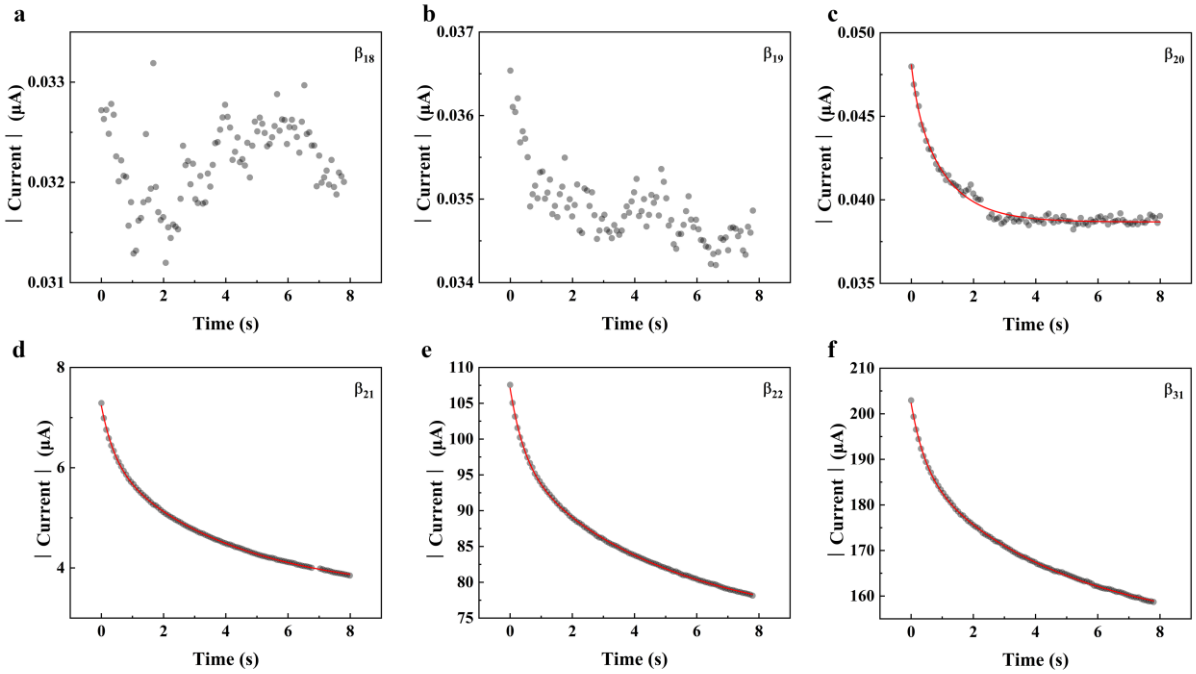

Fig. S7 Double-exponential decay of Au/a-ZATO/Au during switching from HRS to LRS. β_1-β_{31} are the labels of the relaxation processes. (a)–(f) From β_{19} (-1.9 V pulse), the noticeable exponential decay just started to appear in the pulse interval. The gray dots are data points, while the red curve is the fitting result.

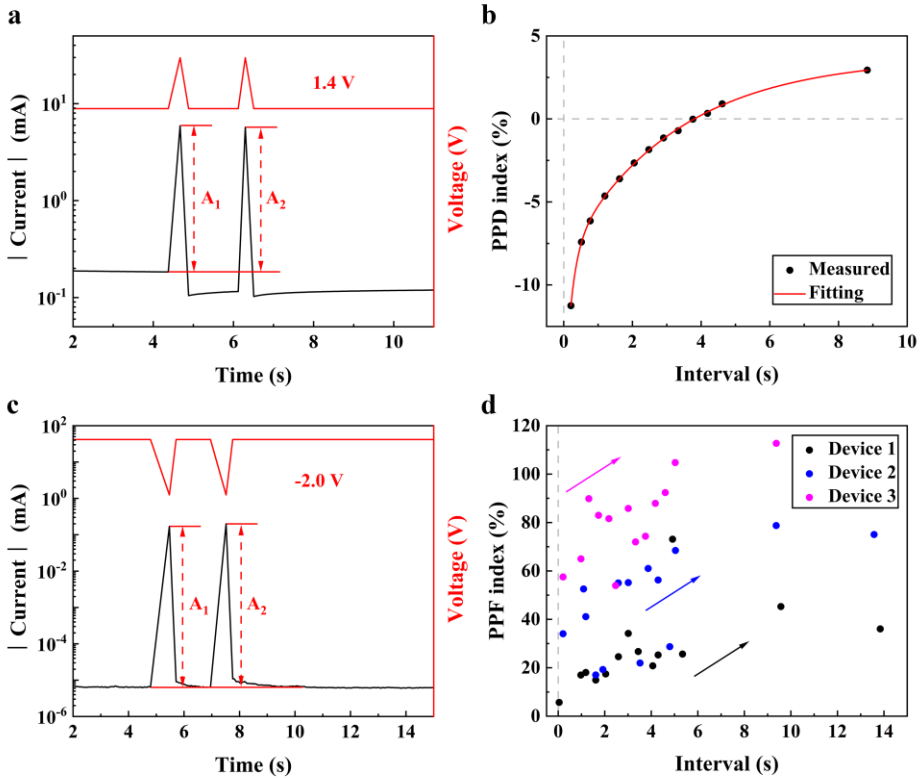

Fig. S8 Paired-pulse depression (PPD) and paired-pulse facilitation (PPF) of Au/a-ZATO/Au. (a) Voltage waveforms and corresponding current responses of two consecutive 1.4 V suppression pulses. A_1 and A_2 represent the difference between the peak current and the current prior to the pulse. (b) Plot PPD index with pulse interval. PPD index is defined as $(A_2\text{-}A_1)/A_1$. Black dots represent measured data. The red curve is the exponential fitting result. (c) Voltage waveforms and corresponding current responses of two consecutive -2.0 V potentiation pulses. (d) Plot PPF index with pulse interval. The index is defined as $(A_2\text{-}A_1)/A_1$. Data measured from 3 devices.

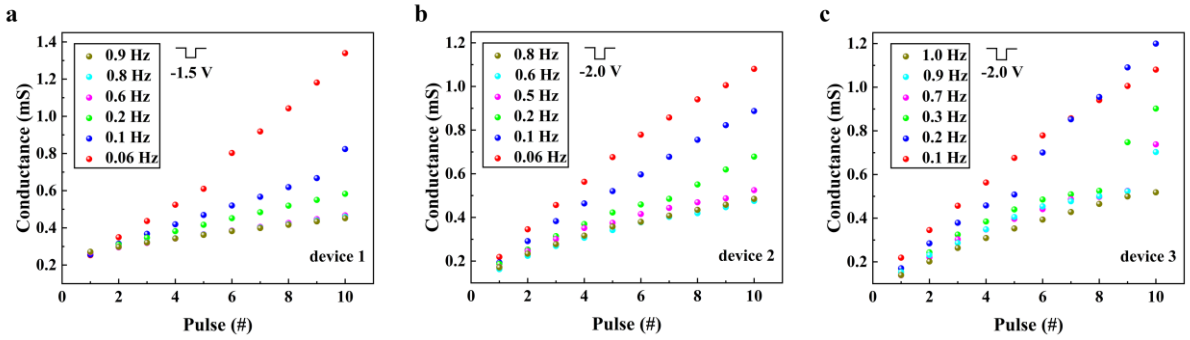

Fig. S9 Abnormal spike-rate-dependent plasticity (SRDP) of Au/a-ZATO/Au. (a) Peak conductance plotted against pulse sequence number. The potentiation pulse amplitude:(a) -1.5 V; (b) and (c) -2.0 V. As the pulse frequency rises, the peak conductance drops.

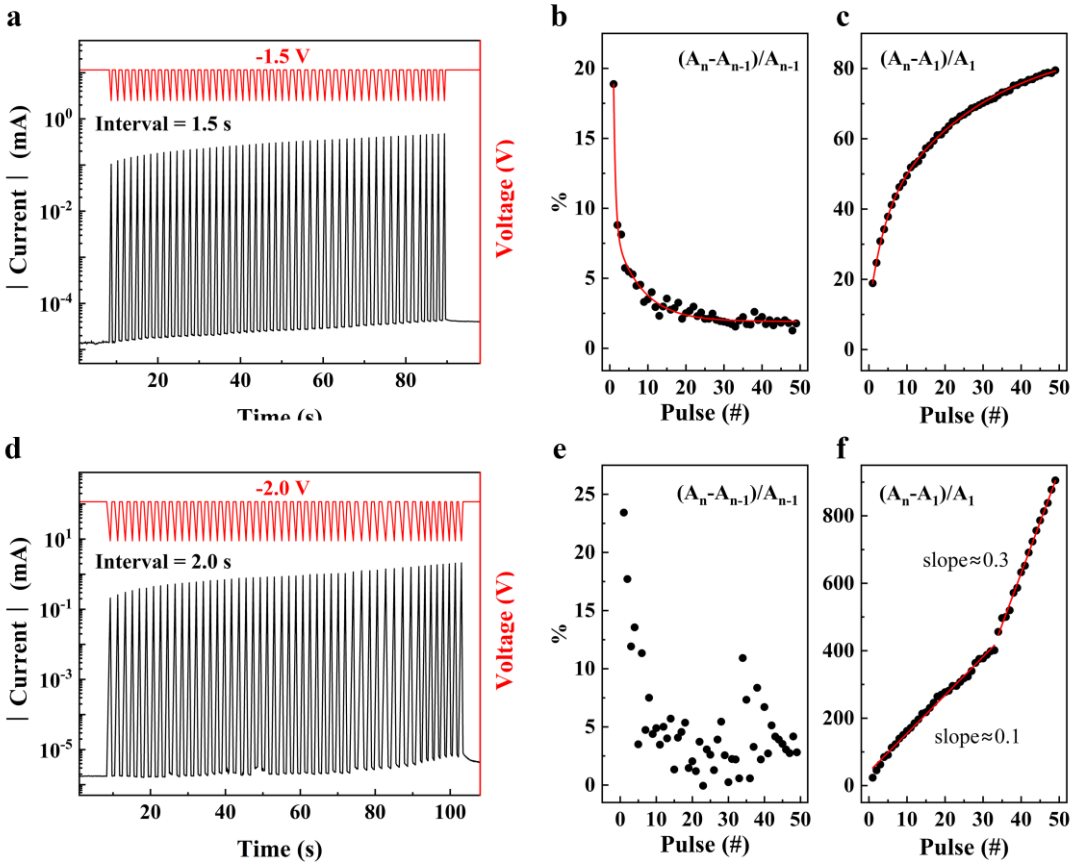

Fig. S10 Peak current saturation characteristics under continuous pulse excitation. (a) Response of 50 consecutive potentiation pulses (-1.5 V, with an interval of 1.5 s). (b) The growth rate of adjacent pulse current is defined as $(A_n\text{-}A_{n-1})/A_{n-1}$. The rate decreases as the number of pulses rises. (c) The growth rate of the subsequent pulse relative to the first pulse current is defined as $(A_n\text{-}A_1)/A_1$, which tends to saturate as the pulse number increases. A_1, A_{n-1} and A_n are the magnitude of peak current, and the subscript numbers indicate the pulse sequence. (d)- (f) Corresponding results when the excitation pulse amplitude is -2.0 V. The increasing slope (from 0.1 to 0.3) in (f) suggests the breakthrough against current saturation.

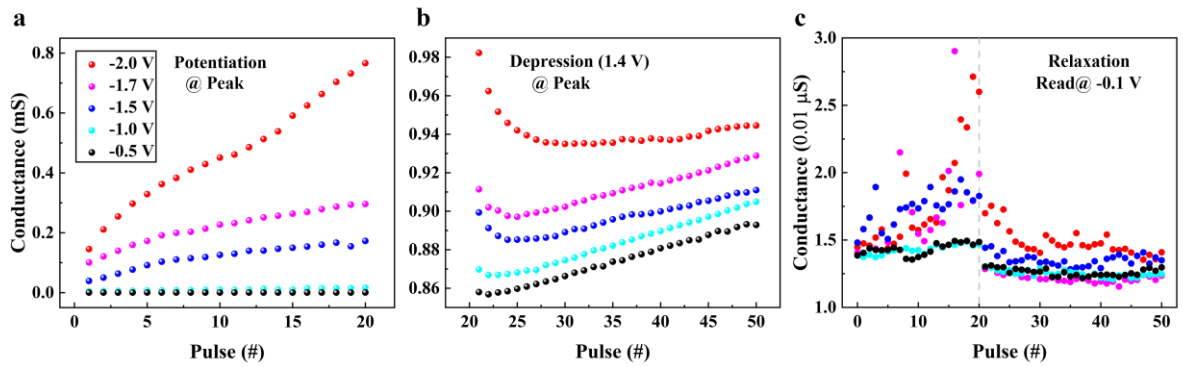

Fig. S11 "Learning-forgetting" test with a pulse group that contains a potentiation pulse train (20 pulses) and a depression pulse train (30 pulses). (a) Peak conductance increases during the potentiation period. 5 excitation pulse amplitudes (-0.5 V, -1.0 V, -1.5 V, -1.7 V and -2.0 V) are selected. (b) Peak conductance in the depression period. (c) Relaxation-conductance during pulse interval. The light gray dotted line marks the boundary between the potentiation and depression period. Read voltage is -0.1 V.

Difference in the potentiation period makes the depression period exhibit significant variations. The peak conductance in the depression period does not simply follow the law of exponential decay, in which there is even a conductance growth component. Note that the peak conductance of depression period is higher than that in the potentiation stage. In particular, even for such small potentiation as -0.5 V and -1.0 V (since their individual stimulus are negligible according to Figure S2), it produces the following distinguishable conductance change: (1) Illustration as the separation of black dots and cyan dots in Figure S11b; (2) The relaxation conductance gap between potentiation and depression at the gray dotted line in Figure S11c. The relaxation-conductance at the end of potentiation is higher than that at the beginning of depression.

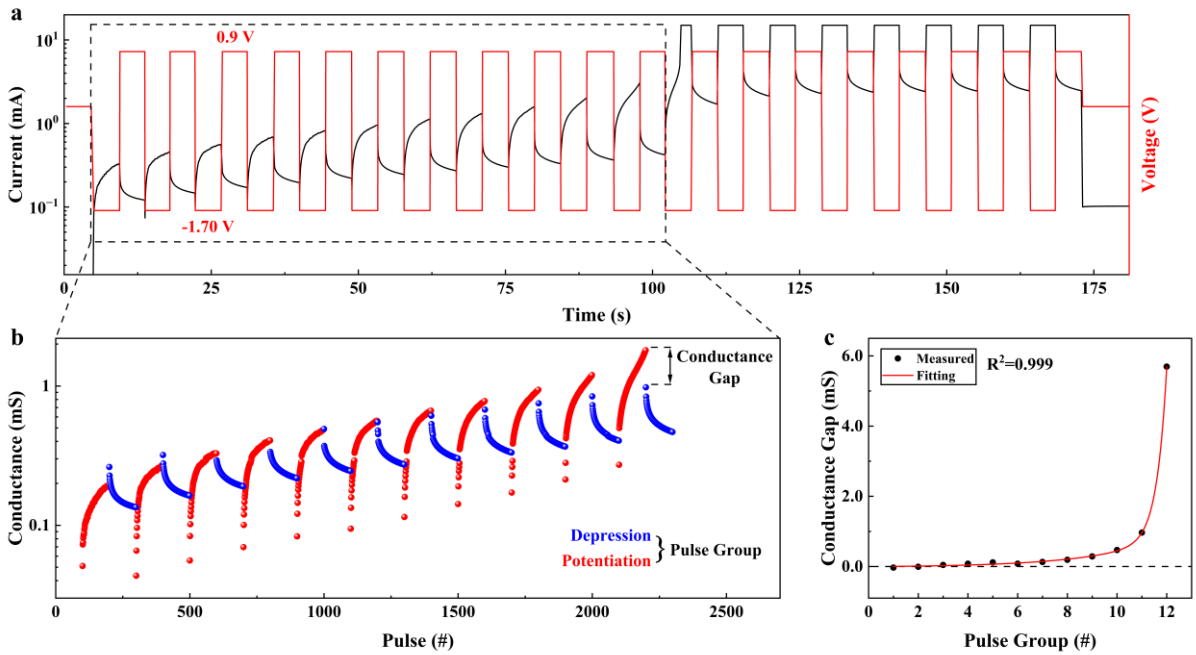

Fig. S12 Consecutive "learning-forgetting" test. A pulse group consists of a potentiation pulse train (-1.7 V, 100 pulses) and a depression pulse train (0.9 V, 100 pulses). Both pulse width and pulse interval are 50 ms. (a) Pulse signal *V-t* diagram (red) and current response *I-t* image. Breakthrough against the current saturation occurs before reaching compliance current. (b) Conductance variation with the number of pulses, corresponding to the dotted box in (a). The potentiation period is marked in red, while blue represents the depression period. Conductance gap is defined as the difference between the peak conductance of the last potentiation pulse and the conductance of the first depression pulse. (c) Plot conductance gap versus pulse group number, which illustrates the transition from negative to positive conductance gap. Black dots are measured values. The fitting function of the red curve is origin BiDoseResp.

The BiDoseResp function from ORIGIN software is as follows:

$$y = A_1 + (A_2 - A_1)\left[\frac{p}{1+10^{(\log x_1 - x)h_1}} + \frac{1-p}{1+10^{(\log x_2 - x)h_2}}\right] \quad (3)$$

Here, y represents the conductance gap in Figure S12 and Figure S13, which is obtained by subtracting the conductance of depression pulse from the conductance of potentiation pulse, and x is serial number of the "learning-forgetting" pulse group. Fitting parameters A_1, A_2, p, x_1, x_2, h_1 and h_2 are with no particular physical meaning.

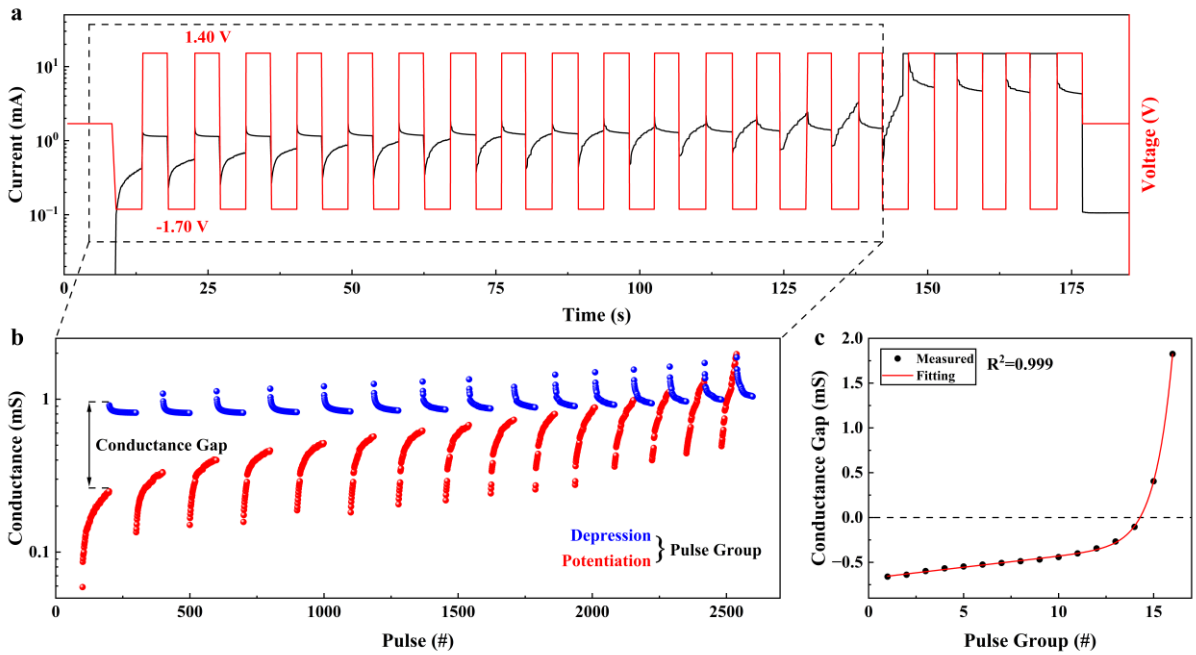

Fig. S13 Consecutive "learning-forgetting" test. Potentiation pulse train (-1.7 V, 100 pulses) and depression pulse train (1.4 V, 100 pulses) are used. Both pulse width and pulse interval are 50 ms. (a) *V-t* (red) and I-t image. Breakthrough against the current saturation occurs before reaching compliance current. (b) Conductance variation with pulse number, corresponding to the dotted box in (a). The black arrow indicates the conductance gap. When the potentiation pulse conductance is smaller than depression pulse, the gap is negative. (c) Conductance gap changes with pulse group number. Black dots are fitted by origin BiDoseResp function.

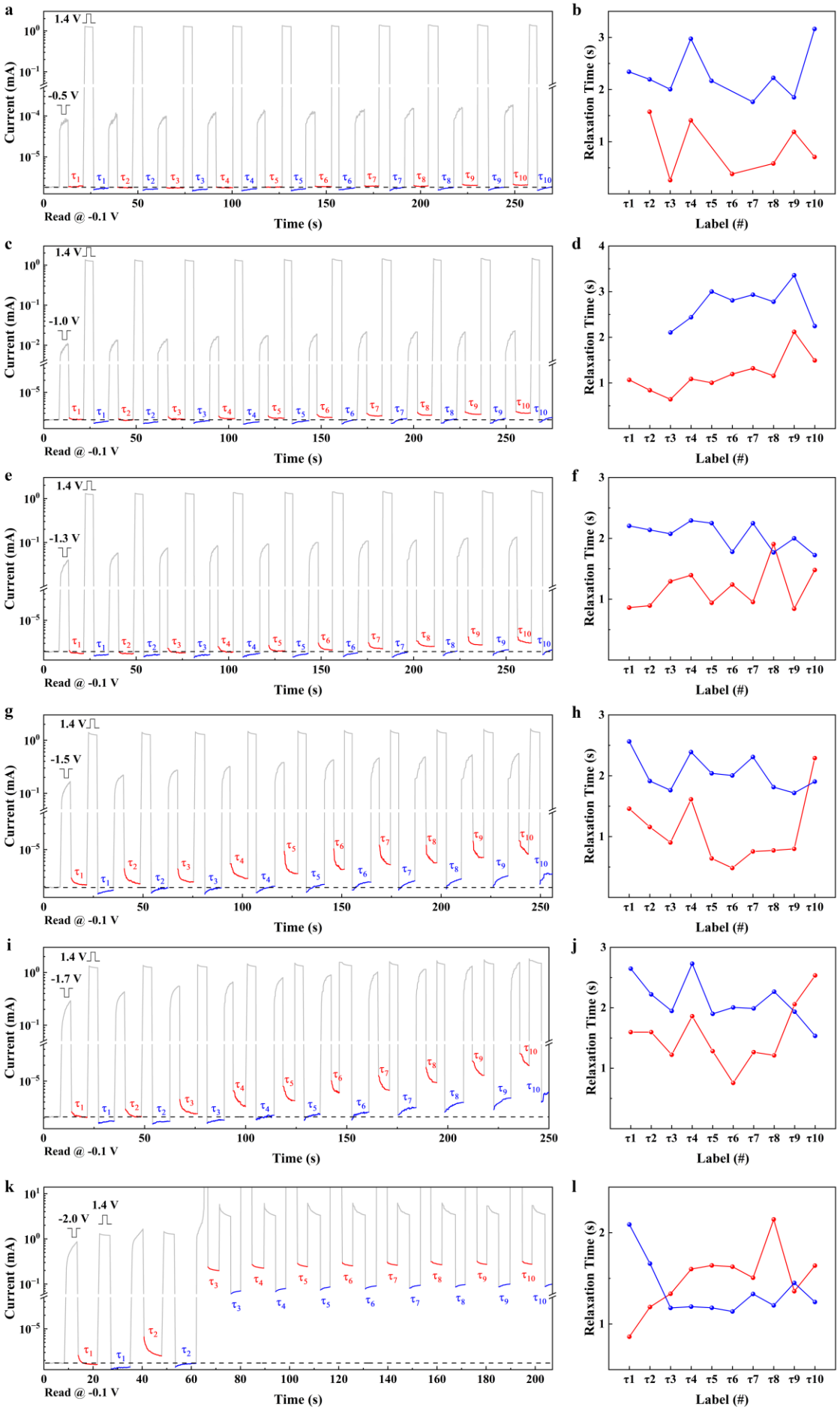
a
1.4 V
-0.5 V
Current (mA)
Read @ -0.1 V
Time (s)
b
Relaxation Time (s)
Label (#)
c
-1.0 V
d
e
-1.3 V
f
g
-1.5 V
h
i
-1.7 V
j
k
-2.0 V
l

Fig. S14 "Learning-forgetting" test with relaxation period. A relaxation time of 8 s was inserted between each potentiation pulse train (100 pulses) and depression pulse train (100 pulses). The depression pulse amplitude is fixed at 1.4 V. (a) *I-t* diagram when the potentiation pulse amplitude is -0.5 V. The black dotted line marks the initial current. The red τ_1-τ_{10} is the time constant obtained by exponential fitting of the relaxation current (red curve) after potentiation. The blue τ_1-τ_{10} is the time constant obtained by logarithmic fitting of the relaxation current (blue curve) after depression. (b) Evolution of the time constant during the test. The potentiation pulse amplitudes for subsequent tests are: (c), (d) -1.0 V; (e), (f) -1.3 V; (g), (h) -1.5 V; (i), (j) -1.7 V. (k) and (l) Potentiation pulse amplitude is -2.0 V. Breakthrough against current saturation occurs before reaching the compliance current (15 mA). The time constant of exponential decay rises, while that of logarithmic relaxation declines.

Note that the relaxation current decays after potentiation and increases after inhibition. The relaxation processes after the potentiation pulse train are fitted by the following expression:

$$I = I_0 + I_1 \exp\left(\frac{-t}{\tau_{\text{red}}}\right) \tag{4}$$

The fitting parameters are I_0 and I_1, and τ_{red} represents the relaxation time constant of exponential decay. Both post-potentiation and post-depression relaxation curves become apparent as the amplitude of the excitation pulse increases. In addition, note that the potentiation peak current is lower than the depression peak current, while the conductance after excitation is higher than that after suppression.

However, a logarithmic expression is required to fit the relaxation process after depression pulse train:

$$I = I_a + (I_b - I_a) \ln\left(\frac{t+c}{\tau_{\text{blue}}}\right) \tag{5}$$

I_{a}, I_{b} and c are fitting parameters. The time constant of logarithmic relaxation is represented by τ_{blue}. It is obvious that Equation 4 and Equation 5 are part of the logarithmic-exponential mixed relaxation. When stronge conductive structures have been constructed, τ_{red} rises and τ_{blue} drops significantly.

Section 3. Cross-sectional microscopic analysis of Au/a-ZnAlSnO/Au

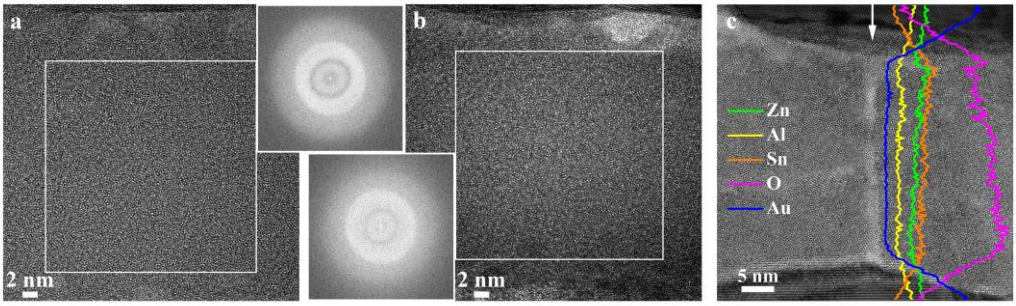

Fig. S15 Cross-sectional high-resolution TEM image of Au/a-ZATO/Au. (a) Pristine device. (b) Device at LRS. The ZATO functional layer has no distinguishable lattice, whose atomic distribution is chaotic and uniform. FFT images from the square selection area only display diffuse rings, indicating amorphous organization. (c) EDS line scan of the LRS device. The oxygen content near BE is slightly more than that near the TE interface.

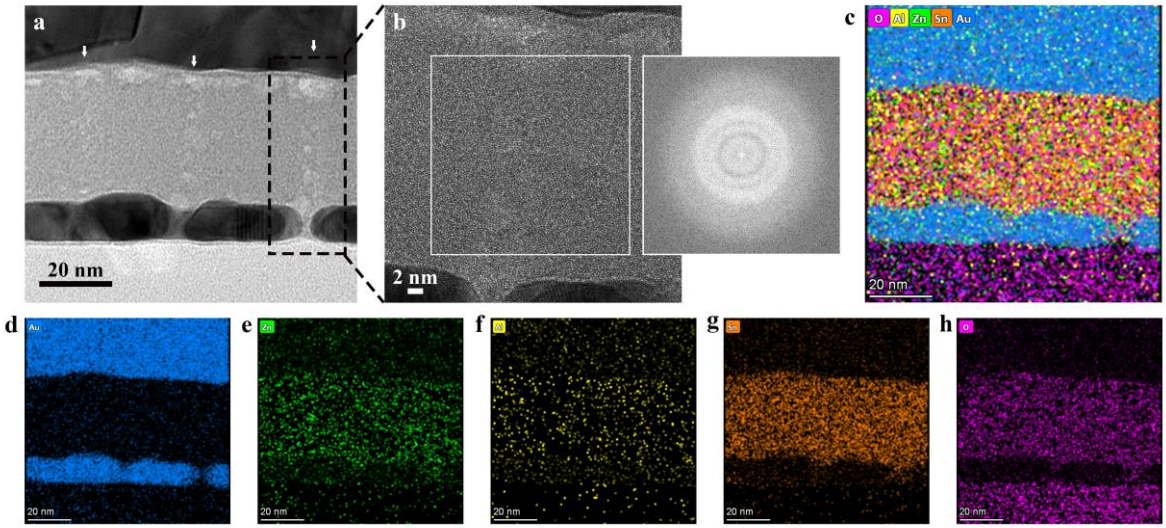

Fig. S16 Residual amorphous filamentous structure in Au/a-ZATO/Au device at LRS. (a) White arrows in the cross-sectional TEM image of the device show that 3 filamentary structures penetrate the functional layer. (b) High-resolution TEM image of the black framed area in (a). The FFT image of the filamentary region enclosed by the white box displays diffuse rings, indicating that the filament is amorphous. (c) Overlay of EDS mapping. d)-h) Distribution of elements Au, Zn, Al, Sn and O on the cross-section.

It should be underlined that the possibility, of which the observed filamentous structure is caused by FIB-induced damage, could be ruled out by comparing the pristine device cross-sections with the LHS device cross-sections.

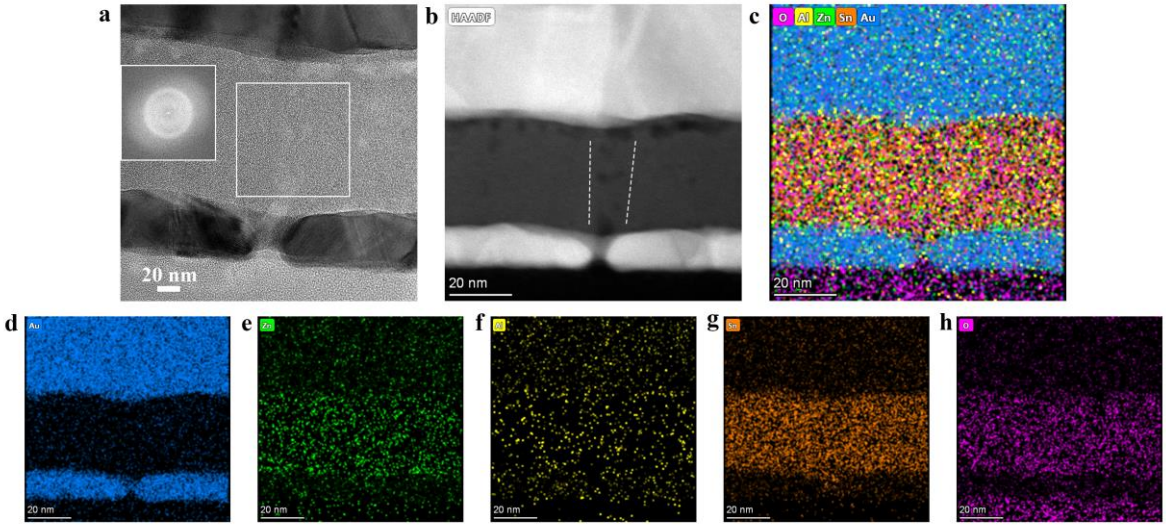

Fig. S17 Residual amorphous filament in LRS device. (a) Cross-section TEM image of Au/a-ZATO/Au. The inset is FFT image from box-selected region of the filamentous structure, indicating that it is amorphous. (b) High-angle annular dark-field (HAADF) image of (a). The filament is marked between the white dotted lines. The contrast of the filamentous structure is lower than the surrounding functional layer. (c) Overlay of EDS mapping. d)-h) Distribution of elements Au, Zn, Al, Sn and O on the cross-section.

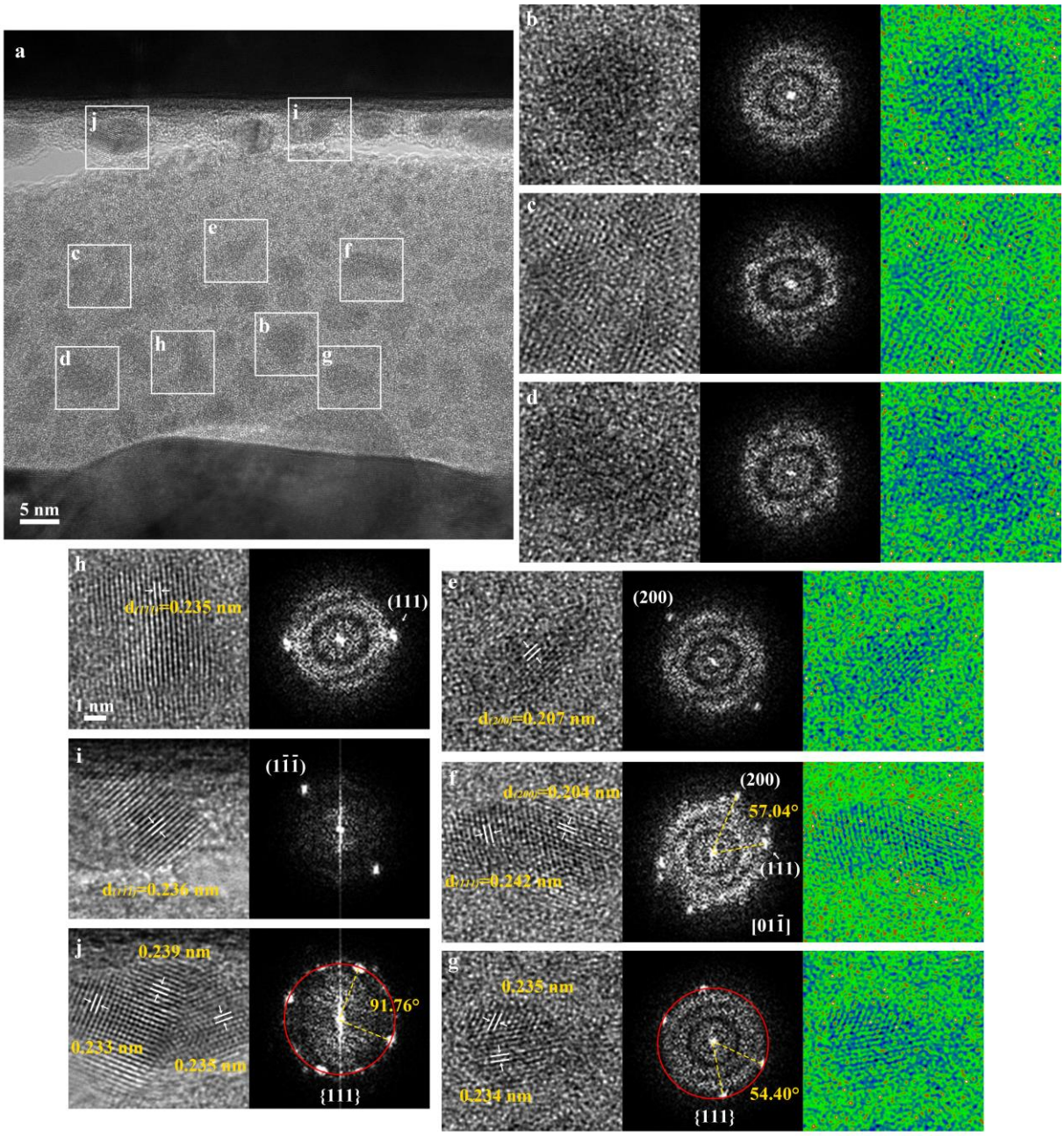

Fig. S18 High-resolution characterization of Au nanoclusters in a-ZATO functional layer. (a) HRTEM image of the device cross-section. Scale bar: 5 nm. White boxes with letter label are the selected FFT regions. (b) HRTEM close-up atomic image of amorphous nanoclusters (left). Scale bar: 1 nm. The corresponding FFT image (middle) displays amorphous diffuse rings. (c) Close-up of a slightly crystalline nanocluster (left) showing a fragmented lattice. The corresponding FFT image (middle) has no obvious pattern. (d) The atomic image of a nanocluster (left) has few resolvable lattices, but the FFT image (middle) shows a pair of bright spots. (e) Atomic image of the nanocluster (left) showing small-scale crystallization with single orientation. The interplanar spacing is 0.207 nm. Combined with the FFT map (middle), it can be resolved as Au (200) single fringes under off-axis condition. (f) Combining the close-up image (left) and the FFT pattern (middle), it could be demonstrated that the interplanar spacing of 0.204 nm is from the Au (200) fringe, while the spacing of 0.242 nm from the Au (111) fringe. Hence, the HRTEM image is taken along the zone axis of [01-1] . Moreover, there are twin-crystal spot near the (111) pattern. g) Atomic image (left) of nanocluster with different orientations. The interplanar spacing (0.234 nm, 0.235 nm) could be resolved as the {111} habit

planes of the Au polycrystal as illustrated in FFT image (middle).The polar colored atomic images on the right side of (b)-(g) highlight the low contrast of Au nanoclusters. (h) The nanocluster close-up (left) and the FFT image (middle) indicate that the single orientation crystalline region corresponds to the Au (111) single fringe with interplanar spacing of 0.235 nm. (i) The nanocluster region can be resolved as Au (1-1-1) single fringe with interplanar spacing of 0.235 nm. (j) The interplanar spacings of the nanocluster region are 0.233 nm, 0.235 and 0.239 nm, which are identified as the {111} habit planes of Au polycrystals as shown in FFT image. The nanocluster close-up images in (b)-(j) were processed by FFT filtering. Note that regardless of the Au crystallinity, the diffuse ring representing amorphous in the FFT image has not disappeared.

Section 4. The logarithmic-exponential mixed relaxation and the device failure process

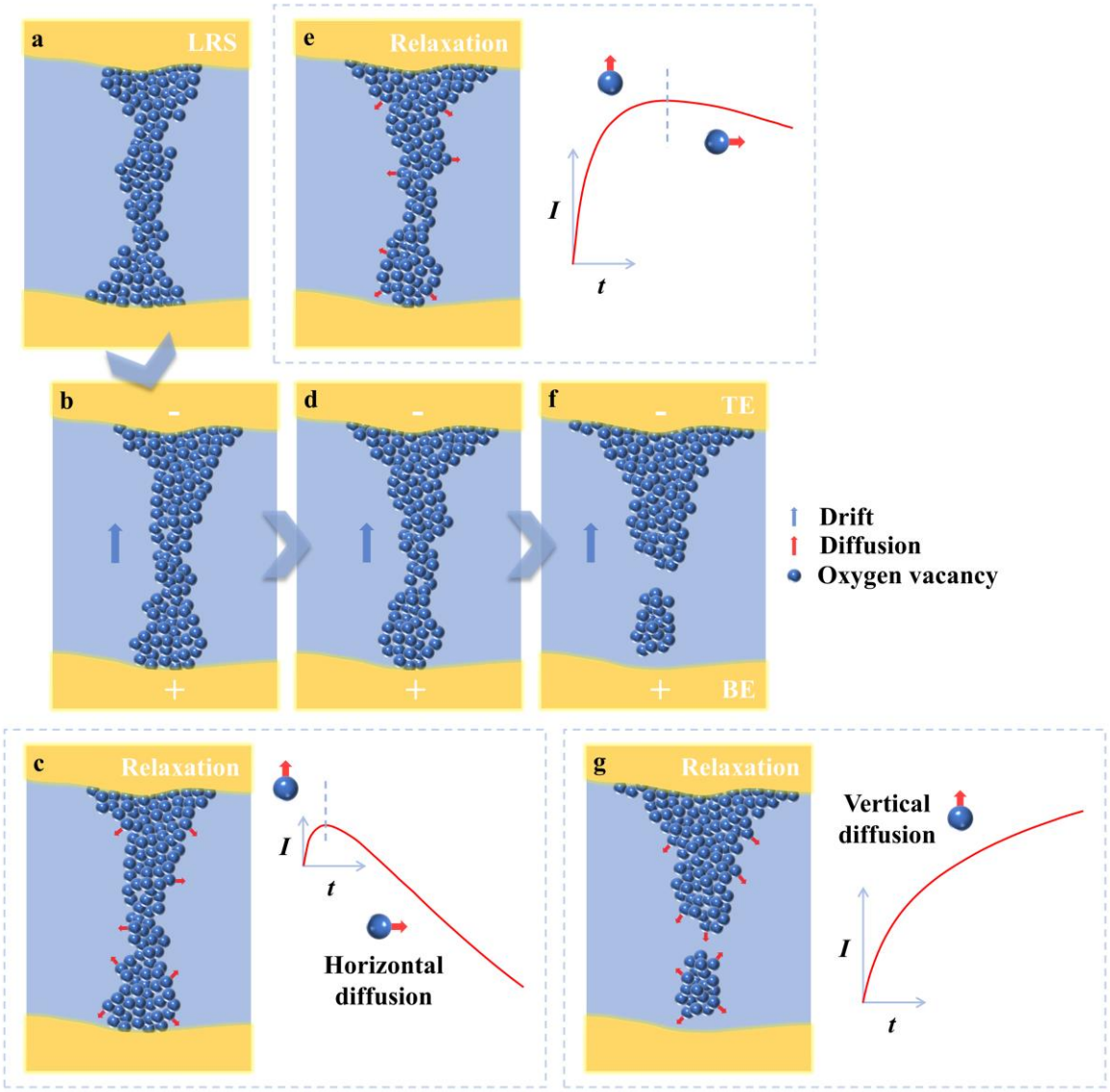

Fig. S19 Schematic diagram of the logarithmic-exponential mixed relaxation of Au/a-ZATO/Au during LRS to HRS switching. (a) Conductive filaments are formed by oxygen vacancies accumulation during switching to LRS. The concentration of oxygen vacancies (blue sphere) is higher than that of surrounding. (b) Geometry of the filament is reorganized due to drift under bias, resulting in contact area decrease between the filament and BE. (c) By removing bias in (b), the diffusion (as shown by red arrow for example) of oxygen vacancies can be divided into vertical and horizontal diffusion component. Vertical diffusion restores the contact area between the filament and BE, causing transient conductance increase. Horizontal diffusion tends to dissolve the filament structure, reducing conductance. The overall conductance mainly sees a gradual decrease during relaxation because the filament structure is still relatively complete. (d) The morphology of the filament changes significantly under continuous bias. The contact area between the filament and BE is smaller than (b) remarkably. Note that the out-diffusion of oxygen vacancies is suppressed by sufficient electric field. (e) During relaxation of (d), vertical diffusion can recover more filament-BE contact area so the conductance rising lasts longer than (c). Horizontal diffusion contributes to the conductance drop continuously since the filament still connect the TE and BE. (f) Finally, the filament is severely deformed to break under bias. (g) The beginning relaxation conductance is

significantly lower than that of (c) and (d). The vertical diffusion at this time helps to reconstruct the filament, resulting in conductance increase. Since the filament broken, horizontal diffusion is not enough to cause further decrease in conductance, so only increasing current could be observed in *I-t* diagram.

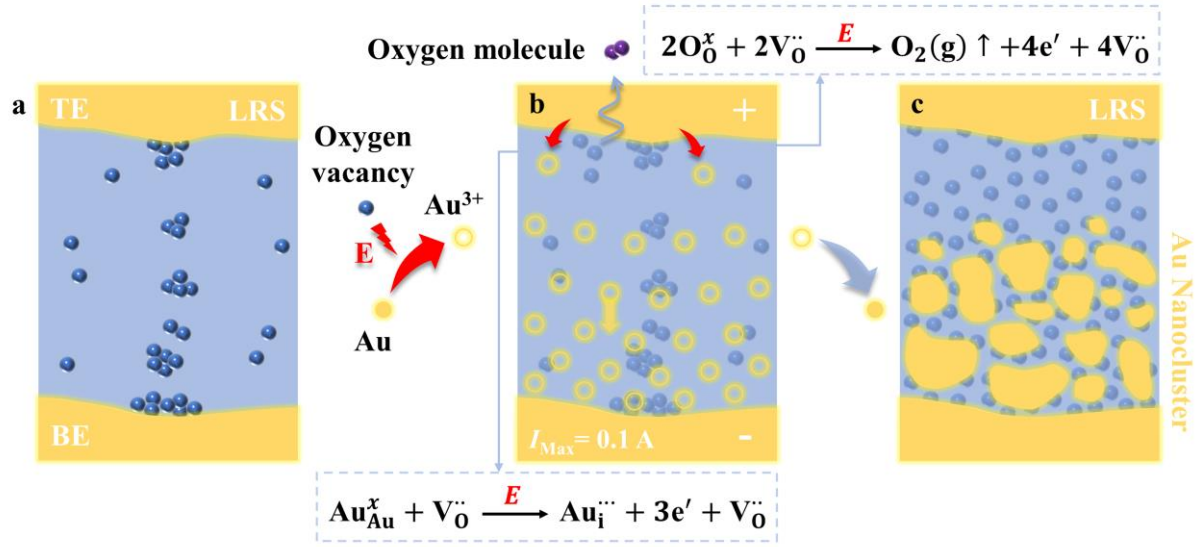

Fig. S20 Au nanocluster generation and oxygen release: schematic failure analysis diagram of Au/a-ZATO/Au under high current condition. (a) Remnant of conductive filament in LRS device after long-term relaxation. (b) The peak current reaches 0.1 A accompanied with the strong field. At TE interface, oxygen ions are oxidized to release oxygen (purple double spheres) under the joint influence of the strong field (represented by red letter "E") and oxygen vacancies (blue spheres), resulting in oxygen content decrease in a-ZATO while oxygen vacancies increase. Simultaneously, oxygen vacancies mediated the oxidation of Au atoms (yellow circles) with the help of strong field at TE interface. Gold cations (yellow hollow circles) drift in a-ZATO along the direction of electric field as indicated by yellow arrow and accumulate nearby BE. (c) By removing bias, gold cations are immediately reduced. Hence, Au nanoclusters after Ostwald ripening are closer to BE. It is difficult to switch LRS into HRS again by bias owning to the enrichment/localization of oxygen vacancies on the surface of Au nanoclusters[7] and the high oxygen vacancies content in the functional layer, resulting in permanent failure of the device.

Oxidation of oxygen ions to oxygen molecular is catalyzed by oxygen vacancies under strong field conditions at the anode interface. The Kröger-Vink notation is expressed as follow:[8]

$$2O_O^x + 2V_O^{\cdot\cdot} \rightarrow O_2(g)\uparrow + 4e' + 4V_O^{\cdot\cdot} \quad (6)$$

Oxygen vacancy without electron filled-in is represented by $V_O^{\cdot\cdot}$, while O_O^x represents bonded oxygen. Obviously, Equation 6 is a positive feedback reaction for the a-ZATO functional layer near anode interface, which indicates that the positive charge concentration in this region rises rapidly. Macroscopic bubble-like bumps could be observed on the cross-junction surface of

damaged devices without resorting to microscopic characterization. Therefore, proper operation of the device requires reasonable compliance current.

The Kröger-Vink notation of Au atom oxidation under stronge field:

$$Au_{Au}^{x} + V_{O}^{\cdot\cdot} \rightarrow Au_{i}^{\cdot\cdot\cdot} + 3e' + V_{O}^{\cdot\cdot} \quad (7)$$

Au_{Au}^{x} stands for gold atom in electrode. The gold cation in a-ZATO is represented by $Au_{i}^{\cdot\cdot\cdot}$. The reaction expressed by Equation 7 is catalyzed by oxygen vacancies as well. In addition, the occurrence of Ostwald ripening demonstrates the limited solid solubility of Au in a-ZATO. The migration of gold is also found in perovskite solar cells, while it is caused by light soaking stress, and moreover, temperature is not able to induce the process alone.[9]

Section 5. Material properties of a-ZnAlSnO with different oxygen-vacancies content

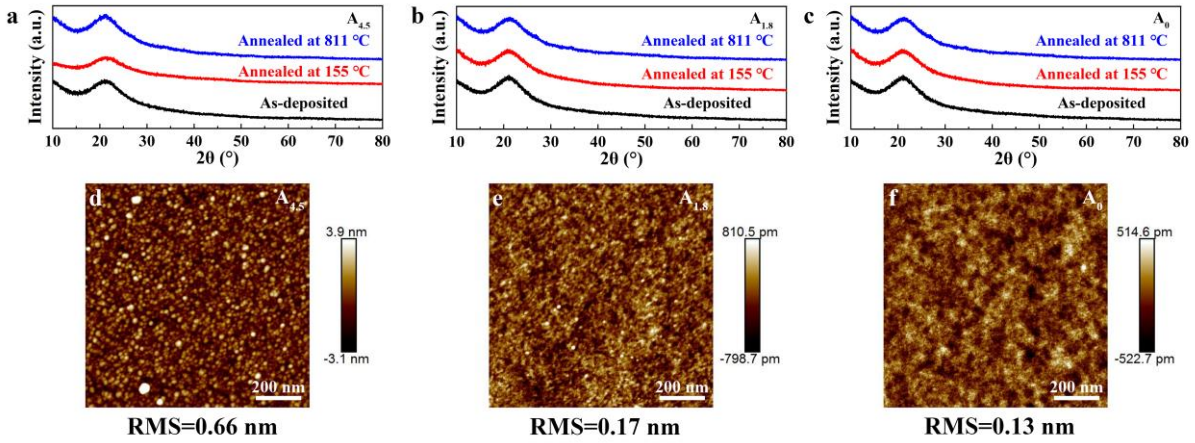

Fig. S21 X-ray diffraction characterization and surface morphology of a-ZATO resistive switching layer. Symbols $A_{4.5}$, $A_{1.8}$ and A_0 represent the oxygen partial pressures of 4.5 Pa, 1.8 Pa and 0 Pa during film deposition, respectively. (a)- (c) XRD spectra of as-deposited films and samples after 30 min annealing (155 °C or 811 °C). (d)- (f) AFM images of each sample in (e).

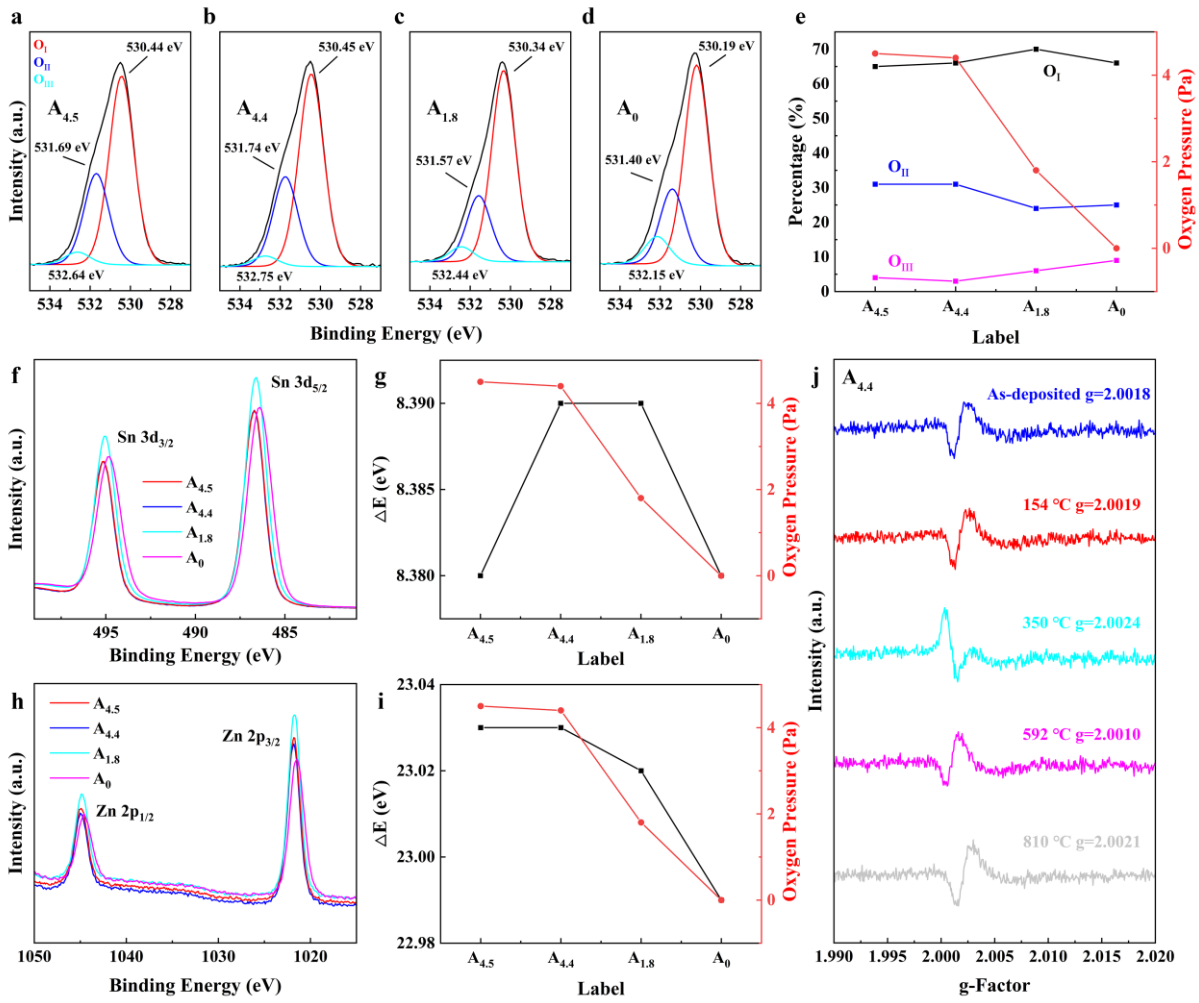

Fig. S22 Oxygen content modulates the pristine chemical state of a-ZATO functional layer. Four typical oxygen pressures of 4.5 Pa, 4.4 Pa, 1.8 Pa and 0 Pa are selected, covering the entire controllable oxygen pressure range of the PLD instrument. The corresponding sample labels are $A_{4.5}$, $A_{4.4}$, $A_{1.8}$ and A_0, respectively. (a)- (d) XPS spectrums of oxygen fitted by Gaussian function. (e) Initial O_I, O_{II}, and O_{III} ratio change with oxygen pressure during preparation. (f) Overlay of Sn 3d spectrums. (g) Variation of Sn 3p chemical shift (ΔE) with oxygen pressure. ΔE is defined as the difference of the split peaks in (f). (h) Overlay of Zn 2p spectrums. (i) Influence of oxygen pressure on Zn 2p ΔE. (j) The electron paramagnetic resonance (EPR) spectrums of the 4.4 Pa samples annealed at different temperatures for 30 min are plotted versus g tensor. Only the $g \approx 2.002$ signal is observable.

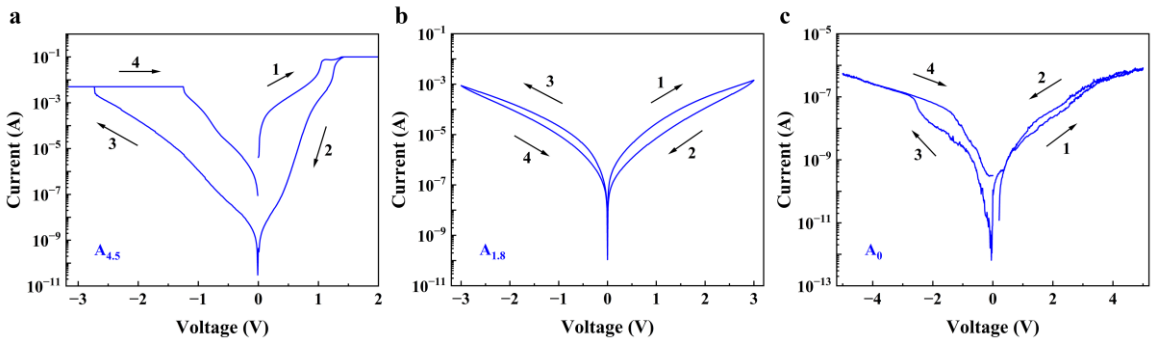

Fig. S23 Pristine oxygen content of the a-ZATO functional layer profoundly affects the device performance. (a) Gradual non-volatile *I-V* (DC) curve of the device with the initial LRS fabricated under 4.5 Pa oxygen pressure. The (b) 1.8 Pa and (c) 0 Pa device exhibit volatility.

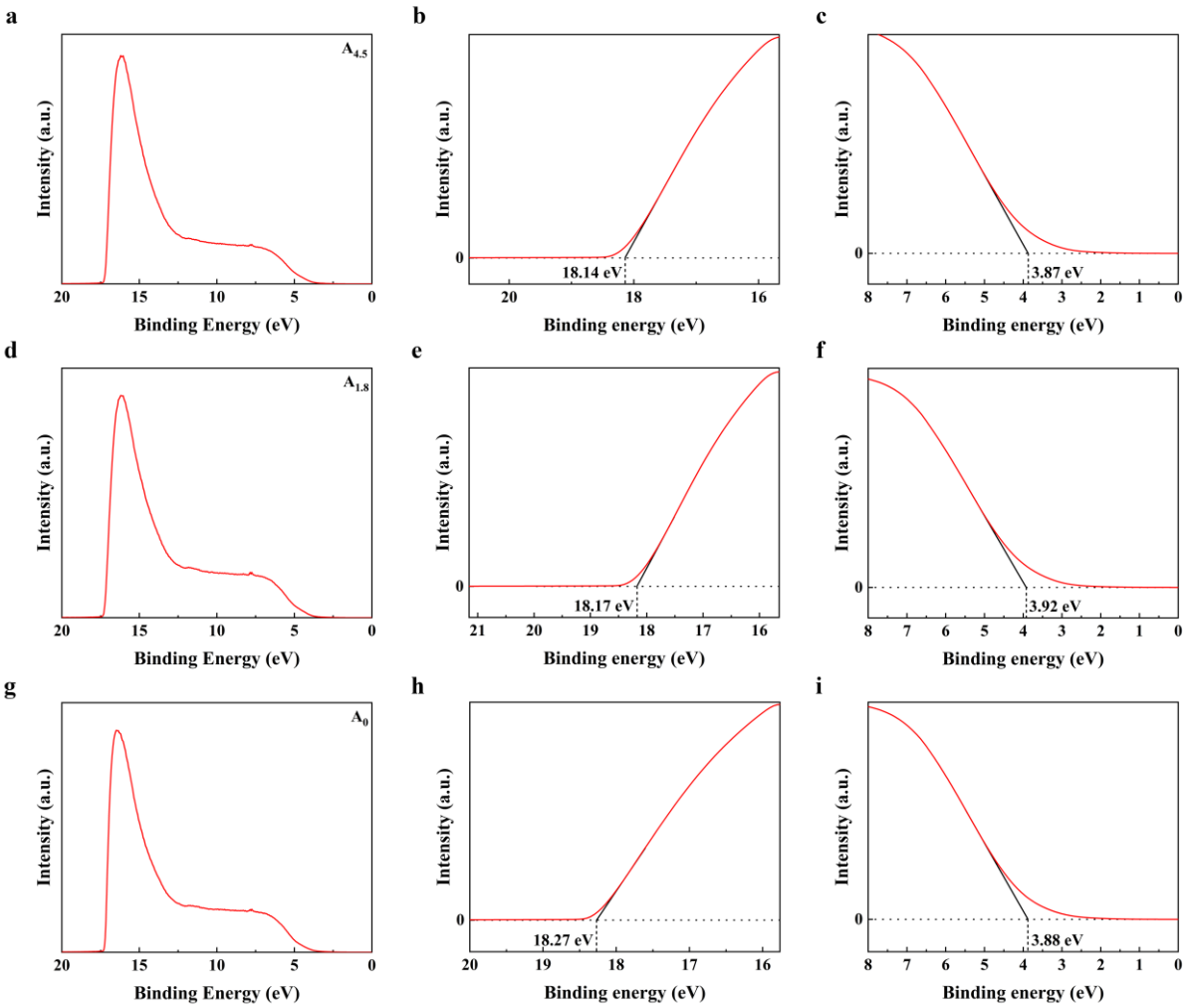

Fig. S24 UV photoelectron spectrums of a-ZATO functional layers prepared at different oxygen pressure. Valence band spectra (left), cut-off edge (middle) and Fermi edge (right) of (a)- (c) 4.5 Pa, (d)- (f) 1.8 Pa and (g)- (i) 0 Pa sample.

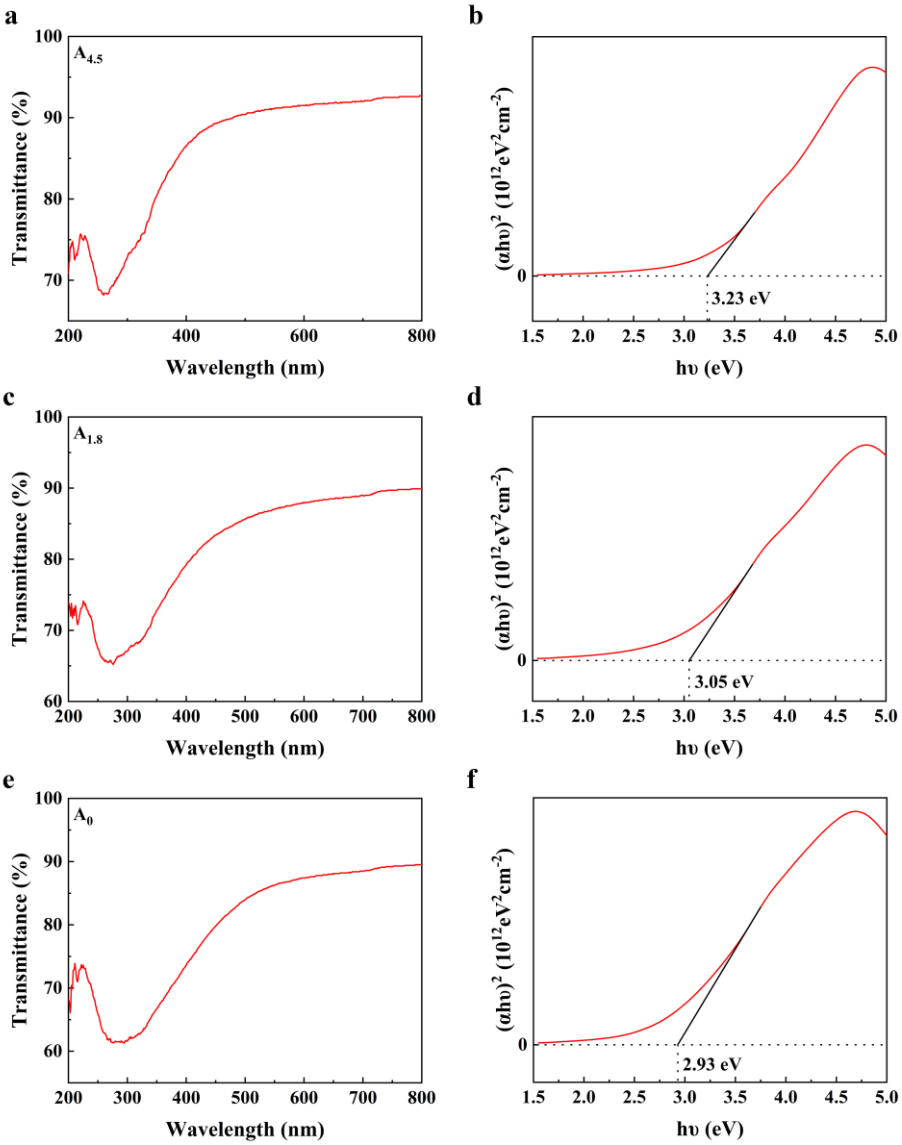

Fig. S25 Optical-bandgap analysis of a-ZATO functional layers prepared at different oxygen pressure. Optical transmittance curve (left) and Tauc plot (right) of (a), (b) 4.5 Pa; (c), (d) 1.8 Pa; (e), (f) 0 Pa sample.

Section 6. Materials and methods

Device fabrication: The resistive switching device Au/amorphous ZnAlSnO/Au (100 nm/30 nm/100 nm) with cross-bar structure was fabricated, whose effective area is 100 ×100 μm^2 at the intersection. First, 10 nm Ti (as adhesive layer) and 100 nm Au bottom electrode (BE) were sequentially deposited by electron beam evaporation on clean double-sided polished quartz substrate, patterned by stainless steel metal mask. Subsequently, 30 nm amorphous ZnAlSnO (a-ZATO) film was deposited on BE at room temperature by pulsed laser deposition (PLD). Oxygen partial pressure of 4.4 Pa was employed and the deposition time was fixed at 5 min. The parameters of pulse laser are: 250 mJ KrF excimer laser (wavelength 248 nm), pulse frequency of 5 Hz and energy density of 3.1 $W \cdot cm^{-2}$. Likewise, metal mask limits the deposition range of functional layers. The oxide ceramic sintered target with an atomic ratio of Zn:Al:Sn=4:2:7 is used for PLD, which was prepared by ZnO, Al_2O_3 and SnO_2 mixed powder. Finally, 100 nm patterned Au top electrode (TE) was evaporated on the a-ZATO layer. Au/a-ZATO/Au cross-bar does not require post-annealing. Other Au/a-ZATO/Au devices were fabricated under different oxygen partial pressures (4.5 Pa, 1.8 Pa, 0 Pa) for comparison, in Supporting Information.

Electrical Measurements: The direct current (DC) and pulse characteristics of Au/a-ZATO/Au were measured by Tektronix 4200A semiconductor parameter analyzer in the atmosphere at room temperature. Pulse mode of SMU module was used for the pulse measurement since the system has not been equipped with a PMU module. A SITE (test group) in the system default contains up to 128 loops. Moreover, there was a power-off between each SITE. In the DC *I-V* measurement, the current range option of the program was set to "AUTO" to ensure that the curve would not be corrected distortedly.

TEM characterization of device cross section: The cross-sectional specimens of devices were prepared by focused ion beam (FIB, Helios 5 UX DualBeam), and the SEM images of device appearance were collected at the same time. The high-resolution transmission electron

microscope (HRTEM) images, small-angle bright-field (BF-S) images and high angle annular dark-field scanning transmission electron microscopy (HAADF STEM) images of the specimens were collected by Thermo Scientific TEM (Talos F200X). Energy dispersive spectroscopy (EDS) mapping and EDS line scan were carried out using the same equipment.

Material Characterization: Amorphous ZnAlSnO thin films were fabricated by PLD on clean quartz substrates at oxygen partial pressures of 0 Pa, 1.8 Pa, 4.4 Pa and 4.5 Pa for material characterization, respectively. The laser parameters (250 mJ, 5 Hz, 3.1 $W \cdot cm^{-2}$, deposition time 5 min) are consistent with that of device preparation. The selected oxygen pressure covers the pressure range of the PLD equipment, representatively.

The surface morphology of the a-ZATO films was characterized by atomic force microscopy (AFM, Bruker) with an area of 1×1 μm^2. X-ray photoelectron spectroscopy (XPS, Thermo Fisher Scientific) with a monochromatic Al Kα source was used to collect the chemical states of Zn, Sn and O in the films. Ultraviolet photoelectron spectroscopy (UPS, Thermo Fisher Scientific) was measured with He I source in order to get the Fermi edge and cut-off edge of the films. The transmittance spectra of the a-ZATO films on the quartz substrate were measured using Shimadzu UV-3600 in the wavelength range of 200-800 nm UV-vis-NIR spectrophotometer. X-ray diffraction (XRD, Panalytical X-Pert-3 Powder) spectra were collected with a monochromatic Cu Kα X-ray source. To investigate the thermal stability of a-ZATO, the XRD samples were divided into as-deposited samples, samples annealed at 155 °C for 30 min and samples annealed at 811 °C for 30 min, where rapid thermal processing (RTP, East Star RTP500) was employed for the post-annealing. Electron paramagnetic resonance (EPR, Bruker EMXPLUS) spectrometer was used to measure single-electron signals of 4.4 Pa a-ZATO thin films which were annealed at different temperatures (as-deposited, 154 °C, 350 °C, 592 °C and 810 °C) for 30 min, respectively.

References

1. H. J. Wan, P. Zhou, L. Ye, Y. Y. Lin, T. A. Tang, H. M. Wu and M. H. Chi, *IEEE Electron Device Letters*, 2010, **31**, 246-248.
2. J. Zhu, T. Zhang, Y. Yang and R. Huang, *Appl. Phys. Rev.*, 2020, **7**, 011312.
3. F. C. Chiu, *Adv. Mater. Sci. Eng.*, 2014, **2014**, 578168.
4. B. Zhao, M. Xiao, D. Shen and Y. N. Zhou, *Nanotechnology*, 2020, **31**, 125201.
5. J. T. Yang, C. Ge, J. Y. Du, H. Y. Huang, M. He, C. Wang, H. B. Lu, G. Z. Yang and K. J. Jin, *Adv. Mater.*, 2018, **30(34)**, 1801548.
6. L. Zhang, H. Yu, C. Xiao, J. Si, H. Xu, W. Zhu and L. Wang, *Advanced Electronic Materials*, 2020, **7**, 2000945.
7. E. Wahlstrom, N. Lopez, R. Schaub, P. Thostrup, A. Ronnau, C. Africh, E. Laegsgaard, J. K. Norskov and F. Besenbacher, *Phys. Rev. Lett.*, 2003, **90**, 026101.
8. F. A. Kröger and H. J. Vink, in *Solid State Physics*, eds. F. Seitz and D. Turnbull, Academic Press, 1956, vol. 3, pp. 307-435.
9. S. Cacovich, L. Cina, F. Matteocci, G. Divitini, P. A. Midgley, A. Di Carlo and C. Ducati, *Nanoscale*, 2017, **9**, 4700-4706.